

Low-Noise and Large-Linear-Dynamic-Range Photodetectors Based on Hybrid-Perovskite Thin-Single-Crystals

Chunxiong Bao, Zhaolai Chen, Yanjun Fang, Haotong Wei, Yehao Deng, Xun Xiao, Lingliang Li, and Jinsong Huang*

Organic–inorganic halide perovskites are promising photodetector materials due to their strong absorption, large carrier mobility, and easily tunable bandgap. Up to now, perovskite photodetectors are mainly based on polycrystalline thin films, which have some undesired properties such as large defective grain boundaries hindering the further improvement of the detector performance. Here, perovskite thin-single-crystal (TSC) photodetectors are fabricated with a vertical p–i–n structure. Due to the absence of grain-boundaries, the trap densities of TSCs are 10–100 folds lower than that of polycrystalline thin films. The photodetectors based on $\text{CH}_3\text{NH}_3\text{PbBr}_3$ and $\text{CH}_3\text{NH}_3\text{PbI}_3$ TSCs show low noise of 1–2 fA $\text{Hz}^{-1/2}$, yielding a high specific detectivity of $1.5 \times 10^{13} \text{ cm Hz}^{1/2} \text{ W}^{-1}$. The absence of grain boundaries reduces charge recombination and enables a linear response under strong light, superior to polycrystalline photodetectors. The $\text{CH}_3\text{NH}_3\text{PbBr}_3$ photodetectors show a linear response to green light from 0.35 pW cm^{-2} to 2.1 W cm^{-2} , corresponding to a linear dynamic range of 256 dB.

Photodetectors based on semiconductors as light absorption and charge transport materials are widely used as light imaging sensors in digital cameras and smartphones due to their small volume, low work voltage, and compatibility for on-chip integration.^[1] Solution-processed semiconductors, such as organic semiconductors and semiconductor quantum dots, are increasingly exploited as alternatives of traditional inorganic semiconductors to meet new photodetection applications, such as flexible, light weight imagers on plastic substrates.^[2,3] Despite the high sensitivity achieved, these devices always suffer from

low response speed due to the low carrier mobility of these solution-processed materials.^[4–6] In recent years, organic–inorganic halide perovskites (OIHPs), a class of solution-processed semiconductor materials with high carrier mobility, have been developed as a new generation of promising materials for optoelectronic devices, including solar cells,^[7–12] light-emitting diodes (LED),^[13–15] solid state lasers,^[16–18] and radiation or photodetectors.^[19–27] The exciting high performances in many optoelectronic devices come from not only their high carrier mobility, but also their large optical absorption coefficient ($\approx 10^5 \text{ cm}^{-1}$), and long carrier recombination lifetime.^[28–30] Perovskite thin-film photodetectors have been intensively investigated in recent years, demonstrating their promising applications as solution-processed photodetectors with high detectivity and fast response

speed.^[20,31] We have demonstrated, for the first time, a perovskite photodetector with the lowest detectable light intensity of sub-pW cm^{-2} , by reducing the device noise with device interface engineering.^[23] The response speed of perovskite thin film photodetectors is limited by the resistance-capacitance (RC) time constant in vertical structure devices, due to the carrier transit distance and large carrier mobility. Recently, we have achieved a high-speed perovskite photodetector with a response time of sub-nanosecond by relieving the constraint from the RC constant of the devices.^[31] Although OIHPs have been extensively studied, almost all the perovskite absorber layers in reported photodetectors are based on polycrystalline films. Further improvement of the performance of the thin-film photodetectors is hindered by the undesired properties of polycrystalline films, such as large-area grain boundaries that are rich in defects.

It was recently shown by us and other groups that perovskite single crystals exhibit notably larger carrier mobility and longer carrier lifetime compared to polycrystalline thin films, because of the tremendously reduced bulk defect densities and the absence of grain boundaries.^[29,30] The outstanding transport properties of perovskite single crystals make them promising materials to further improve the performance of perovskite photodetectors. First, the absence of pin-holes and

Dr. C. Bao, Dr. Z. Chen, Dr. Y. Fang, Dr. H. Wei, Y. Deng, X. Xiao, L. Li, Prof. J. Huang
Department of Mechanical and Materials Engineering
University of Nebraska-Lincoln
Lincoln, NE 68588-0656, USA
E-mail: jhuang2@unl.edu, jhuang@unc.edu
Prof. J. Huang
Department of Applied Physical Sciences
University of North Carolina
Chapel Hill, NC 27599, USA



The ORCID identification number(s) for the author(s) of this article can be found under <https://doi.org/10.1002/adma.201703209>.

DOI: 10.1002/adma.201703209

grain boundaries in single crystals can eliminate the leakage path of currents in single-crystal devices, leading to a lower device noise and further improving the detection sensitivity; second, the longer carrier recombination lifetime in single crystals can improve the device response to strong light. However, previously reported perovskite single-crystal photodetectors always exhibit low sensitivity and slow response speed, which is mainly caused by the unpassivated surface defects and the too-large thickness of the bulky crystals.^[32–35]

Here we study the performance of vertical structured p–i–n photodetectors based on OIHP thin single crystals (TSCs). The OIHP TSCs with thickness of several to tens micrometers and lateral size up to millimeters were grown directly on substrates that are covered with defect passivating hole transport layers.^[36] The TSCs show lower trap density and longer carrier recombination lifetime than optimized polycrystalline thin films. Photodetectors based on these TSCs show ultra-low dark current, leading to a very small noise equivalent power (NEP). Besides, these photodetectors show high photoresponsivity, high specific detectivity, large linear dynamic range (LDR), and high response speed.

Perovskite TSCs used in this study were grown directly on nonwetting hole transport layer coating substrates with a space confine method.^[36] The hydrophobic poly(bis(4-phenyl)(2,4,6-trimethylphenyl)amine) (PTAA) allows the quick diffusion of ions in the confined space, and thus enables the growth of perovskite TSCs with lateral size from hundreds of micrometers all the way up to several millimeters. **Figure 1a,b** shows the X-ray diffraction (XRD) spectra of $\text{CH}_3\text{NH}_3\text{PbBr}_3$ (MAPbBr₃) and $\text{CH}_3\text{NH}_3\text{PbI}_3$ (MAPbI₃) crystals integrated from the 2D XRD patterns (insets), indicating MAPbBr₃ and MAPbI₃ thin crystals are grown along the [100] orientation. The XRD spectra of crystal powders shown in Figure S1 in the Supporting Information demonstrate the pure perovskite phase of the crystals. The 2D XRD patterns shown in the insets of Figure 1a,b consist of isolated spots without continuous arc, indicating their single crystal nature. The photographs of the perovskite TSCs on substrates in the insets of Figure 1a,b show that MAPbBr₃ and MAPbI₃ exhibit square and hexagonal shape, which conformed to the symmetry of the crystal lattice. The lateral sizes of the TSCs are about 2–5 mm, while the thicknesses of the TSCs determined by step profiler are about several to tens micrometers. The devices reported here were based on TSCs with thickness of $\approx 10\ \mu\text{m}$ (Figure S2, Supporting Information).

The optical properties of the perovskite TSCs were further investigated. The absorption spectra of MAPbBr₃ and MAPbI₃ TSCs show sharp absorption edges at 558 and 824 nm, respectively (Figure S3a,b, Supporting Information). Bandgaps extracted from Tauc plots (insets of Figure S3a,b in the Supporting Information) show values of 2.26 and 1.54 eV for MAPbBr₃ and MAPbI₃ TSCs, respectively. The optical bandgaps of the TSCs are slightly larger than the values reported for bulk single crystals,^[24,30] which can be attributed to the much smaller thickness of our TSCs. The smaller optical bandgaps of thick bulk single crystals come from the increase of absorption of the band tail states or the smaller indirect band-gap. The steady state photoluminescence (PL) spectra show narrow peaks at 545 and 776 nm for MAPbBr₃ and MAPbI₃ TSCs. The PL spectrum of the MAPbI₃ TSC is consistent with the result

of MAPbI₃ bulk single crystals we reported previously.^[30] However, the PL spectrum of the MAPbBr₃ TSC differs from our previously reported results from MAPbBr₃ bulk single crystals, which showed that PL spectra of MAPbBr₃ bulk single crystals always have two peaks.^[37] One is generated on the top surface, and the other is the filtered PL after self-absorption and multiple reflections.^[37] The absence of the filtered PL peak indicates the PTAA substrate basically quenched the PL at that interface.

The vertical-structure p–i–n photodetectors were fabricated with perovskite TSCs as light absorbing layers. The schematic structure of the photodetectors is shown in Figure 1c. The PTAA layer that acted as nonwetting layer in the crystal growth process is the hole transport layer in the device; a 20-nm-thick C60 and 8 nm thick bathocuproine (BCP) was deposited on the crystals by thermal evaporation as the electron transport and hole blocking layers, respectively. Figure 1d shows typical photo- and dark- current density–voltage (*J*–*V*) curves of perovskite TSC photodetectors. The photocurrents at reverse bias close to 0 V keep almost constant, which indicates that the photogenerated electrons and holes can be efficiently extracted at 0 V bias, and the photodetectors are self-powered. Both types of devices show low dark current, 2.0×10^{-9} and $1.8 \times 10^{-7}\ \text{A cm}^{-2}$ for MAPbBr₃ and MAPbI₃ TSC devices at $-0.3\ \text{V}$, which are lower than the MAPbI₃ polycrystalline thin film devices with similar device structure.^[31] To evaluate the stability of the dark current under continuous bias, we measured the dark current at different fixed bias for about 80 s. The typical dark current density–time curves are shown in Figure S4 in the Supporting Information. The average and standard deviation of the dark current for the MAPbBr₃ based devices at different bias are shown in Figure 1d. The dark current measured at fixed voltage ($1.36 \times 10^{-9}\ \text{A cm}^{-2}$ at $-0.3\ \text{V}$) is lower than that measured with scanning voltage. The lower dark current of the single crystal photodetectors benefits from the absence of pin-holes and grain boundaries, which are always leakage paths in thin-film devices. Moreover, our previous work showed that grain boundaries in polycrystalline perovskite film are primary location of the trap states in addition to the crystal surfaces.^[38] The grain-boundary-free single crystals are expected to have smaller trap state density (tDOS), which can further reduce the $1/f$ noise of the photodetectors.^[23,39] Figure 1e shows the tDOS measured with the thermal admittance spectroscopy method, which shows that the tDOS of the MAPbBr₃ TSC photodetector is smaller than that of the MAPbI₃ TSC photodetector. The tDOS of the MAPbI₃ TSC photodetector are 10–100 folds smaller than that of the photodetector based on polycrystalline thin films (500 nm) which has a same structure with the TSC devices (Figure S5a, Supporting Information). The *J*–*V* curves of the thin film device in the dark and under illumination are shown in Figure S5c in the Supporting Information, which shows similar photocurrent but much larger dark current compared to the TSC devices.

The carrier recombination lifetime is an important factor to determine the photoresponse linearity of a photodetector especially in the strong light region. To evaluate the carrier recombination lifetime, we then performed the transient photovoltage (TPV) measurements to evaluate the photogenerated carrier lifetime. The photovoltage decay curves of MAPbBr₃ and MAPbI₃ TSC photodetectors under green (532 nm) bias light

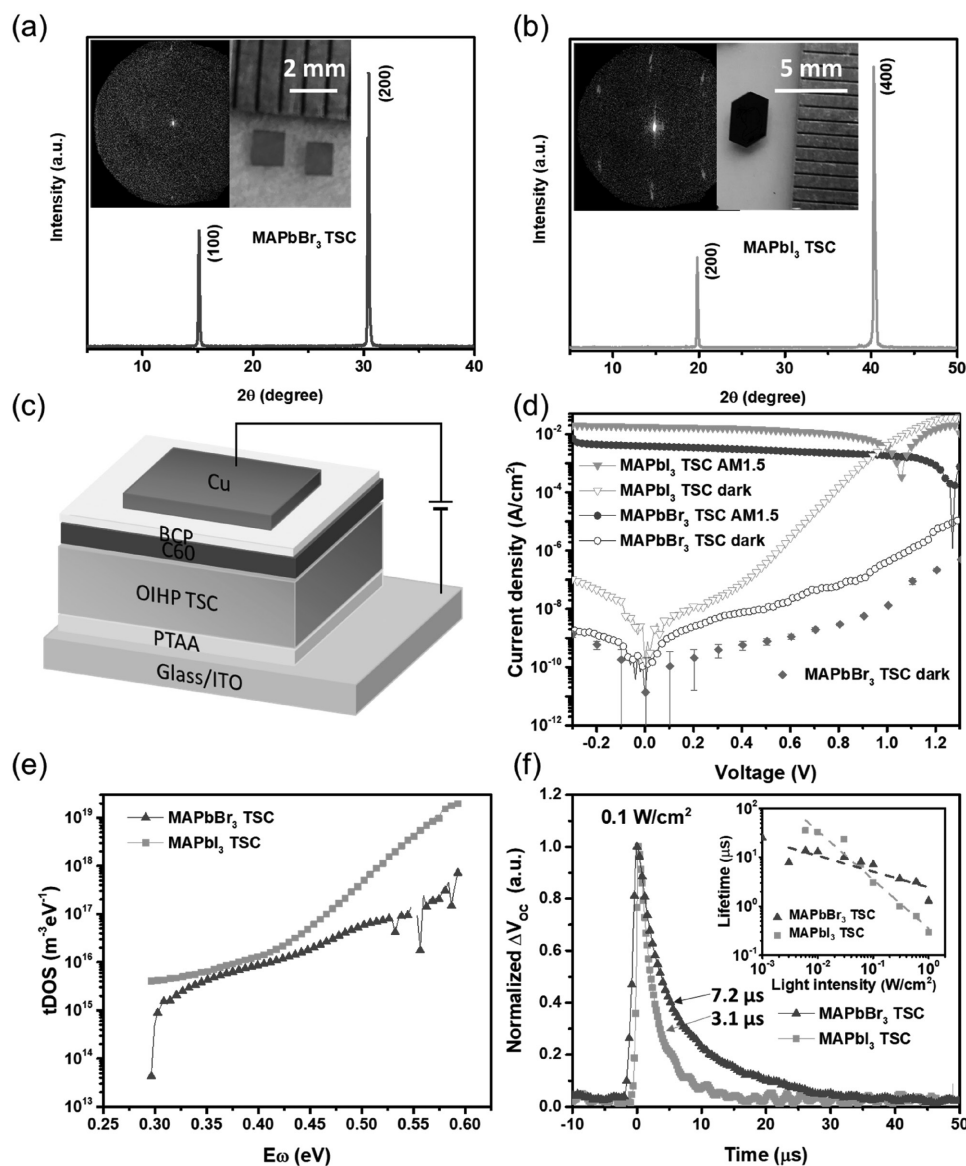


Figure 1. X-ray diffraction spectra of a) MAPbBr₃ and b) MAPbI₃ thin-crystals integrated from the 2D X-ray diffraction patterns. Insets are the 2D X-ray diffraction patterns along with the photographs of the thin crystals. c) Schematic structure of the photodetector based on perovskite TSCs with a vertical p-i-n structure. d) Current density of the perovskite TSC photodetectors under dark and one sun (AM1.5). The line + symbol curves were measured with scanning voltage, the curve with error bar (diamond) was measured with fixed voltage point-by-point. e) Trap-density-of-states (tDOS) curves of devices based on MAPbBr₃ and MAPbI₃ TSCs. f) Transient photovoltage (TPV) of photodetectors based on MAPbBr₃ and MAPbI₃ TSCs under green light illumination of 0.1 W cm⁻². The TPV decay time of devices based on MAPbBr₃ and MAPbI₃ TSCs under 0.1 W cm⁻² green light are measured to be 7.2 and 3.1 μs, respectively. Inset: the plots of decay time of the TPV measured at various bias light intensities.

with intensity of 0.1 W cm⁻² are demonstrated in Figure 1f. The curves can be fitted with exponential decays with characteristic time constants of 7.2 and 3.1 μs for MAPbBr₃ and MAPbI₃ TSC-based devices. The inset of Figure 1f shows the carrier lifetime of the photodetectors under various light intensities from 10⁻³ to 1 W cm⁻². Carrier lifetime of MAPbI₃ TSC devices is obviously much longer than that of polycrystalline thin film devices (Figure S5b, Supporting Information), which benefits from the absence of the defective grain boundary in TSCs. The carrier lifetime of the devices decrease as the light intensity increase, because the increase of the photogenerated

carrier concentration will enhance the recombination of the carriers.

The low dark current of the perovskite TSC photodetectors contributed to the low noise of the devices, which is an essential factor that determines the sensitivity of a photodetector. Generally, shot noise and thermal noise dominate the total noise in perovskite photodetector.^[23] In principle, when a self-powered photodetector work at 0 V bias in dark situation, there is no current flowing through the device due to the lack of a driving force for the carrier to drift. The shot noise is determined by dark current

$$i_{n,s} = \sqrt{2eI_d B} \quad (1)$$

where e is the element charge, I_d is the dark current, and B is the bandwidth, the shot noise for the device at 0 V bias could be negligible and the thermal noise should be the dominant noise. The thermal noise can be expressed as

$$i_{n,t} = \sqrt{\frac{4k_B T B}{R}} \quad (2)$$

where k_B is the Boltzmann constant, T is the temperature, and R is the resistance of the device. Based on the differential resistance at 0 V extracted from the dark current in Figure 1d, the thermal noises are calculated to be 0.43 fA Hz^{-1/2} for MAPbBr₃ and 1.7 fA Hz^{-1/2} for MAPbI₃ TSC devices. We measure the noise current of the devices using a lock-in amplifier and low noise preamplifier. The noise spectra of MAPbBr₃ and MAPbI₃ TSC devices at frequencies from 1 to 10 Hz are shown in Figure 2a. The devices show small noise currents below 10 fA Hz^{-1/2} and reach 1.4 and 1.8 fA Hz^{-1/2} at the frequency of 8 Hz to MAPbBr₃ and MAPbI₃.

The external quantum efficiency (EQE) of the perovskite TSC photodetectors measured under 0 V bias are shown in Figure 2b. The EQEs of the MAPbI₃ TSC device are between 50% and 62%, corresponding to a responsivity from 0.17 to 0.32 A W⁻¹ in the wavelength range from 400 to 780 nm, while the EQEs of the MAPbBr₃ single crystal device are between

52% and 60%, corresponding to a responsivity from 0.17 to 0.26 A W⁻¹ in the wavelength range from 400 to 540 nm, in accordance with the absorption spectra in Figure S3a,b in the Supporting Information.

Based on the measured dark current noise (i_n) and the responsivity (R_λ) of the devices, the NEP of the device can be calculated according to the expression

$$\text{NEP} = \frac{i_n}{R_\lambda} \quad (3)$$

The NEP of MAPbBr₃ and MAPbI₃ based devices for a bandwidth of 1 Hz at 532 nm are calculated to be 5.4 and 7.0 fW, respectively. To compare with photodetectors with different active area, the device active area should be considered. Thus, we can obtain the specific detectivity (D^*)

$$D^* = \frac{\sqrt{AB}}{\text{NEP}} \quad (4)$$

where A is the device area. The D^* to various wavelength are calculated and shown in Figure 2c,d. The D^* of the perovskite TSC based photodetectors are above 1×10^{12} cm Hz^{1/2} W⁻¹ from 350 nm to the absorption onset wavelength, with the peak value of about 1.5×10^{13} cm Hz^{1/2} W⁻¹, which are much larger than that of MAPbI₃ polycrystalline thin-film-based photodetector,^[22,23] and comparable to the commercial silicon

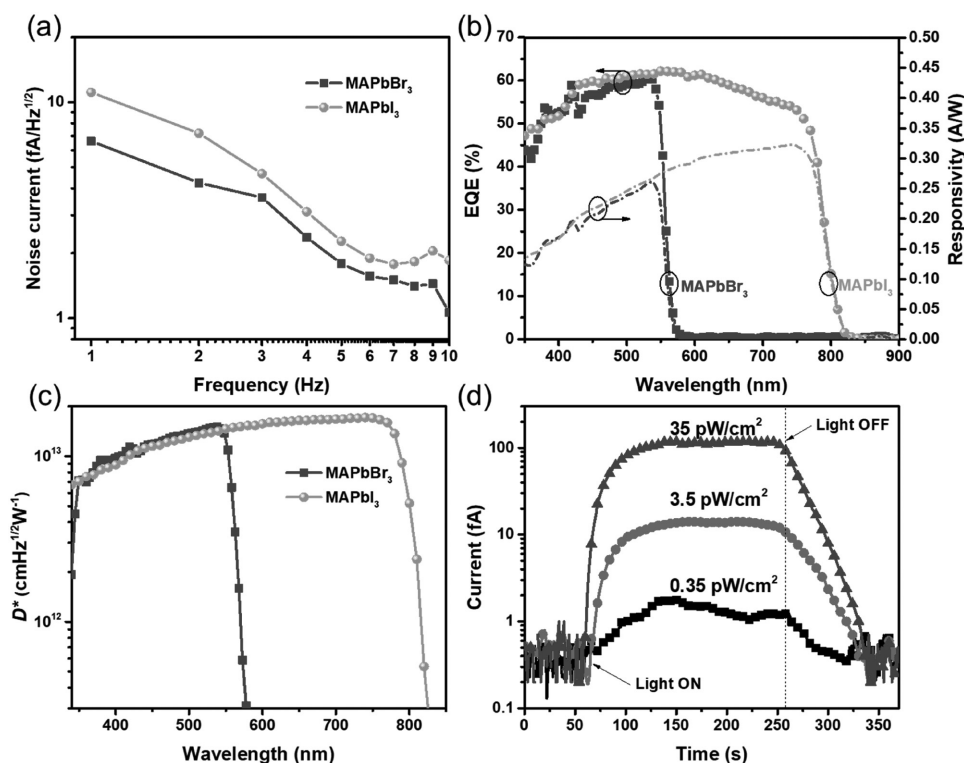


Figure 2. a) Noise current of photodetectors based on MAPbBr₃ and MAPbI₃ TSCs at 0 V bias voltage. b) External quantum efficiency (EQE) and responsivity spectra of photodetectors based on MAPbBr₃ and MAPbI₃ TSCs. c) Specific detectivity (D^*) of devices based on MAPbBr₃ and MAPbI₃ TSCs measured at 0 V bias and 8 Hz. d) The current output of the MAPbBr₃ TSC device to green light with intensities of 0.35, 3.5, and 35 pW cm⁻².

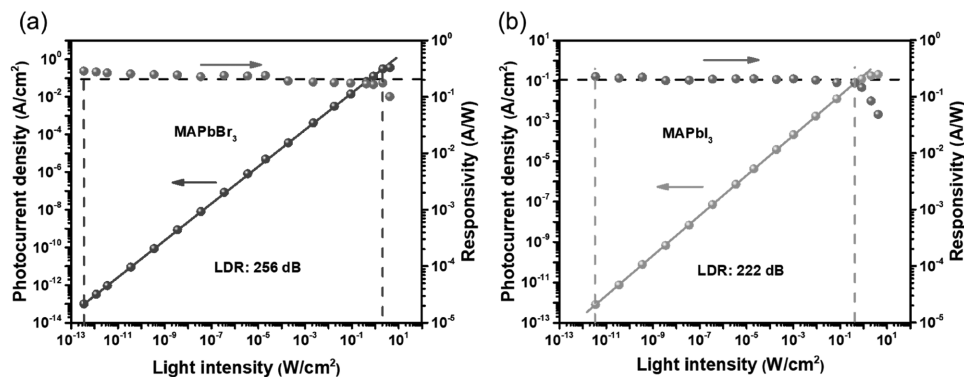


Figure 3. The dynamic-range characterization of photodetectors based on a) MAPbBr₃ and b) MAPbI₃ TSCs at 0 V with green-light illumination of various light intensities. The solid line is a linear fitting to the data. The corresponding responsivity are shown in the figures with Y axis on the right.

photodetector. The high D^* of the perovskite TSC photodetectors indicates that the photodetectors can detect a very-low light intensity. The measured current response of MAPbBr₃ TSC photodetector to weak light shown in Figure 2d directly demonstrates that MAPbBr₃ TSC photodetector can detect weak light intensity of 0.35 pW cm⁻². The rising and falling edges of the curves in Figure 2d are limited from the slow response of the lock-in amplifier to weak signal.

Most photodetector applications, such as image sensors and illumination meters, need to extract the intensity of the detection light from the photocurrent over a wide light-intensity range, so having a constant responsivity over a wide range of light intensity is an important property for a photodetector. The LDR is a figure-of-merit for photodetectors to characterize the light intensity range in which the photodetectors have a constant responsivity, which is always expressed as

$$\text{LDR} = 20 \log \frac{P_{\text{sat}}}{P_{\text{low}}} \text{ or } 10 \log \frac{P_{\text{sat}}}{P_{\text{low}}} \quad (5)$$

where P_{sat} (P_{low}) is the light intensity when the incident light intensity stronger (weaker) than which the photocurrent begins to deviate from linearity. The LDR of MAPbBr₃ and MAPbI₃ TSC photodetectors were measured by recording the photocurrent of the devices under green light (532 nm) with various light intensities modulated by neutral density optical filters at a frequency of 8 Hz. The results are exhibited in Figure 3. By linearly fitting the data we found that the R -squared (coefficient of determination) of the linear fitting for MAPbBr₃ and MAPbI₃ devices are 0.99995 and 0.99996, which are very close to 1, indicating the perfect linearity of the data. It can be seen that the photocurrent of the MAPbBr₃ TSC device have a linear response from 0.35 pW cm⁻² to 2.1 W cm⁻², corresponding to a LDR of 256 dB, which is larger than that (222 dB) of MAPbI₃ TSC device and represents the largest reported LDR for perovskite photodetectors. From Figure 3 we can also see that the responsivity of both MAPbBr₃ and MAPbI₃ TSC devices keep almost constant at the linear response range, which confirms the measured large LDR of perovskite TSC photodetectors. A large LDR of a detector need a high specific detectivity for a small NEP and a large saturation light intensity to define the upper limit. The saturation at which the photocurrent begins

to deviate from linear relationship with light intensity, should be determined by the ratio of carrier lifetime and the carrier extracted time.^[22] The carrier recombination lifetime in the TSC photodetectors remained to be long even under high light intensity. As shown in Figure 1f, the carrier lifetime for the MAPbBr₃ TSC photodetector under 1 W cm⁻² was still larger than 1 μs, which is much larger than the charge extracted time (≈100 ns as shown below). Therefore, the MAPbBr₃ TSC photodetector can keep linear response to light intensity higher than 1 W cm⁻². The longer carrier recombination lifetime should be ascribed to the lower defect state density of perovskite TSCs. In addition, the 200-folds lower photogenerated carrier concentration in the TSCs devices than in polycrystalline thin film devices should also contribute to the longer charge recombination lifetime.

The response speed is another important parameter of a photodetector. The response speed of the perovskite TSC photodetectors was measured by the transient photocurrent (TPC) method, with a 4 ns wide pulse laser (337 nm) as the light source. Figure 4a shows the TPC decay curves of the MAPbBr₃ and MAPbI₃ TSC devices. By fitting the TPC decay curves with the single exponential decay function, the response time of the MAPbBr₃ and MAPbI₃ TSC devices were derived to be 100 and 300 ns, respectively. The capacitance of the devices measured with a precision inductance-capacitance-resistance (LCR) meter was tens pF, corresponding to a RC constant of about several ns ($R = 50 \Omega$), which is far smaller than the measured response time, so the response time of the device is dominated by the carrier transit times in the perovskite crystal layers.

For a photodetector, the transit-time-limited 3 dB cutoff frequency can be expressed as^[40]

$$f_{3\text{dB}} \approx \frac{0.443}{\tau_{\text{tr}}} \quad (6)$$

where τ_{tr} is the transit time of the device, which can be estimated from the TPC as 100 and 300 ns for MAPbBr₃ and MAPbI₃ TSC devices, respectively. Based on the transit time, the 3 dB cutoff frequencies of MAPbBr₃ and MAPbI₃ TSC devices can be calculated to be 4.4 and 1.5 MHz. The frequency responses of the devices were studied with a square wave voltage driven LED as the light source and an oscilloscope

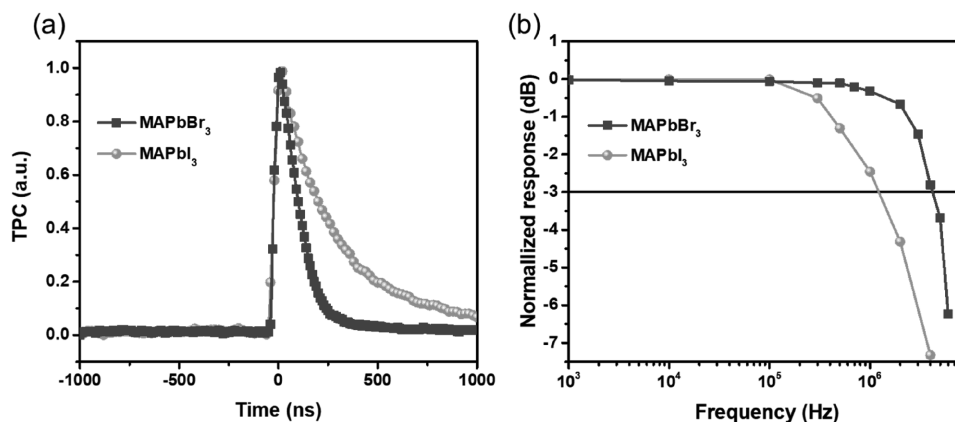


Figure 4. a) Transient photocurrent and b) frequency response of photodetectors based on MAPbBr₃ and MAPbI₃ TSCs. The TPC decay time of MAPbBr₃- and MAPbI₃-based devices were measured to be 100 and 295 ns, respectively.

recording the photocurrents of the devices. The photocurrents of MAPbBr₃ and MAPbI₃ TSC devices under different frequencies modulated light are shown in Figure S6 in the Supporting Information. From the amplitude of the photocurrent we can obtain the frequency response of the devices (Figure 4b). As shown in Figure 4b, the 3 dB cutoff frequencies of MAPbBr₃ and MAPbI₃ devices are 4.2 and 1.2 MHz, which in accordance with that calculated from the transit time.

In summary, we have demonstrated the solution-processed high-performance photodetectors based on MAPbBr₃ and MAPbI₃ perovskite thin single crystals with a vertical p-i-n device structure. Due to the low defect density and grain-boundary-free nature of the single crystals, the thin single crystal photodetectors show low dark current, low noise equivalent power, and high specific detectivity. A sub-pW cm⁻² weak light detection limitation can be obtained with MAPbBr₃ thin single crystal photodetector. Besides, a record linear dynamic range of 256 dB were obtained for MAPbBr₃ single crystal photodetectors due to the much longer carrier recombination lifetime of the single crystal devices under strong light. Our study demonstrates the great application potential of perovskite thin single crystals in high-performance photodetectors.

Experimental Section

Device Fabrication: The TSCs of perovskite were in situ grown on nonwetting substrates with a space-limiting method as previously reported.^[36] Briefly, a thin layer of PTAA (≈20 nm) was firstly spin coated on cleaned ITO glass. A certain amount of 1.5 M MAPbBr₃ (MAPbI₃) precursor solution was dropped onto the PTAA coating ITO glass and covered with another PTAA coating ITO glass. The TSCs can be obtained after growth at certain temperature (85 °C for MAPbBr₃ and 120 °C for MAPbI₃). Then, layers of C60 (20 nm), BCP (8 nm) were thermal deposited successively as electron transport and hole-blocking layer, respectively. Finally, an 80 nm Cu layer was thermal evaporated with a mask to define the device active area as 0.6–1.5 mm².

Device Characterization: X-ray diffraction of the thin crystal and powder ground from the crystals was performed on a Bruker-AXS D8 Discover diffractometer with 2D area detector. Absorption spectra of the TSCs were recorded on a UV-vis spectrophotometer (Thermo Scientific, Evolution 201) with a blank ITO glass as baseline.

Steady photoluminescence spectra were measured using an iHR320 photoluminescence spectroscopy with a 402 nm continuous wave laser as excited light. *J*-*V* curves of the devices under illumination and dark were collected with a Keithley 2400 source meter. The irradiation was from a solar simulator (Oriel 67005, 150 W), which was calibrated to AM1.5G (100 mW cm⁻²) by a silicon photodetector (Hamamatsu S1133). tDOS was derived from capacitance–frequency and capacitance–voltage curves which were measured using a precision LCR meter (Agilent E4980A). Transient photocurrent and photovoltage were recorded by an oscilloscope with input resistances of 50 Ω and 1 MΩ, respectively, when the device was illuminated with a pulse laser whose wavelength is 337 nm and pulse width is 4 ns. Transient photocurrent was measured in dark and transient photovoltage was measured under bias light from a 532 nm continuous wave laser with various intensities. The external quantum efficiencies of the devices were measured using a Newport QE measurement system, with the under-tested device kept at zero bias voltage and the incident monochrome light was modulated to 8 Hz with a chopper. The noise current of the devices was measured using a lock-in amplifier (Stanford Research System, SR830). During the measurement, the device was posited in a dark metal box and the connecting wires were shielded with aluminum foil to reduce the noise produced by the electromagnetic interference. To measure the frequency response of the devices, a square wave voltage driven fast response green LED was used as light source, and the photocurrents of the devices were recorded by an oscilloscope.

Supporting Information

Supporting Information is available from the Wiley Online Library or from the author.

Acknowledgements

C.B. and Z.C. contributed equally to this work. This work was supported by the Department of Homeland Security under Award No. 2014-DN-077-ARI069-03 and the National Science Foundation under Award No. ECCS-1608610.

Conflict of Interest

The authors declare no conflict of interest.

Keywords

hybrid perovskites, linear dynamic range, photodetectors, sensitivity

Received: June 8, 2017

Revised: July 31, 2017

Published online: August 28, 2017

- [1] E. R. Fossum, *IEEE Trans. Electron Devices* **1997**, *44*, 1689.
- [2] X. Gong, M. Tong, Y. Xia, W. Cai, J. S. Moon, Y. Cao, G. Yu, C.-L. Shieh, B. Nilsson, A. J. Heeger, *Science* **2009**, *325*, 1665.
- [3] G. Konstantatos, I. Howard, A. Fischer, S. Hoogland, J. Clifford, E. Klem, L. Levina, E. H. Sargent, *Nature* **2006**, *442*, 180.
- [4] Z. Bao, A. Dodabalapur, A. J. Lovinger, *Appl. Phys. Lett.* **1996**, *69*, 4108.
- [5] H. Sirringhaus, N. Tessler, R. H. Friend, *Science* **1998**, *280*, 1741.
- [6] L. Shen, Y. Lin, C. Bao, Y. Bai, Y. Deng, M. Wang, T. Li, Y. Lu, A. Gruverman, W. Li, J. Huang, *Mater. Horiz.* **2017**, *4*, 242.
- [7] M. Lee, J. Teuscher, T. Miyasaka, T. N. Murakami, H. J. Snaith, *Science* **2012**, *338*, 643.
- [8] H.-S. Kim, C.-R. Lee, J.-H. Im, K.-B. Lee, T. Moehl, A. Marchioro, S.-J. Moon, R. Humphry-Baker, J.-H. Yum, J. E. Moser, M. Grätzel, N.-G. Park, *Sci. Rep.* **2012**, *2*, 591.
- [9] H. Zhou, Q. Chen, G. Li, S. Luo, T.-b. Song, H.-S. Duan, Z. Hong, J. You, Y. Liu, Y. Yang, *Science* **2014**, *345*, 542.
- [10] M. Liu, M. B. Johnston, H. J. Snaith, *Nature* **2013**, *501*, 395.
- [11] A. Mei, X. Li, L. Liu, Z. Ku, T. Liu, Y. Rong, M. Xu, M. Hu, J. Chen, Y. Yang, M. Grätzel, H. Han, *Science* **2014**, *345*, 295.
- [12] Q. Dong, J. Song, Y. Fang, Y. Shao, S. Ducharme, J. Huang, *Adv. Mater.* **2016**, *28*, 2816.
- [13] Z.-K. Tan, R. S. Moghaddam, M. L. Lai, P. Docampo, R. Higler, F. Deschler, M. Price, A. Sadhanala, L. M. Pazos, D. Credgington, F. Hanusch, T. Bein, H. J. Snaith, R. H. Friend, *Nat. Nanotechnol.* **2014**, *9*, 687.
- [14] H. Cho, S.-H. Jeong, M.-H. Park, Y.-H. Kim, C. Wolf, C.-L. Lee, J. H. Heo, A. Sadhanala, N. Myoung, S. Yoo, S. H. Im, R. H. Friend, T.-W. Lee, *Science* **2015**, *350*, 1222.
- [15] Y.-H. Kim, H. Cho, J. H. Heo, T.-S. Kim, N. Myoung, C.-L. Lee, S. H. Im, T.-W. Lee, *Adv. Mater.* **2015**, *27*, 1248.
- [16] G. Xing, N. Mathews, S. S. Lim, N. Yantara, X. Liu, D. Sabba, M. Grätzel, S. Mhaisalkar, T. C. Sum, *Nat. Mater.* **2014**, *13*, 476.
- [17] F. Deschler, M. Price, S. Pathak, L. E. Klintberg, D. D. Jarausch, R. Higler, S. Hüttner, T. Leijtens, S. D. Stranks, H. J. Snaith, M. Atatüre, R. T. Phillips, R. H. Friend, *J. Phys. Chem. Lett.* **2014**, *5*, 1421.
- [18] H. Zhu, Y. Fu, F. Meng, X. Wu, Z. Gong, Q. Ding, M. V Gustafsson, M. T. Trinh, S. Jin, X.-Y. Zhu, *Nat. Mater.* **2015**, *14*, 636.
- [19] X. Hu, X. Zhang, L. Liang, J. Bao, S. Li, W. Yang, Y. Xie, *Adv. Funct. Mater.* **2014**, *24*, 7373.
- [20] L. Dou, Y. (M.) Yang, J. You, Z. Hong, W.-H. Chang, G. Li, Y. Yang, *Nat. Commun.* **2014**, *5*, 5404.
- [21] R. Dong, Y. Fang, J. Chae, J. Dai, Z. Xiao, Q. Dong, Y. Yuan, A. Centrone, X. C. Zeng, J. Huang, *Adv. Mater.* **2015**, *27*, 1912.
- [22] Q. Lin, A. Armin, D. M. Lyons, P. L. Burn, P. Meredith, *Adv. Mater.* **2015**, *27*, 2060.
- [23] Y. Fang, J. Huang, *Adv. Mater.* **2015**, *7*, 2804.
- [24] Y. Fang, Q. Dong, Y. Shao, Y. Yuan, J. Huang, *Nat. Photonics* **2015**, *9*, 679.
- [25] S. Yakunin, M. Sytnyk, D. Kriegner, S. Shrestha, M. Richter, G. J. Matt, H. Azimi, C. J. Brabec, J. Stangl, M. V. Kovalenko, W. Heiss, *Nat. Photonics* **2015**, *9*, 444.
- [26] H. Wei, Y. Fang, P. Mulligan, W. Chuirazzi, H.-H. Fang, C. Wang, B. R. Ecker, Y. Gao, M. A. Loi, L. Cao, J. Huang, *Nat. Photonics* **2016**, *10*, 333.
- [27] X. Zhang, S. Yang, H. Zhou, J. Liang, H. Liu, H. Xia, X. Zhu, Y. Jiang, Q. Zhang, W. Hu, X. Zhuang, H. Liu, W. Hu, X. Wang, A. Pan, *Adv. Mater.* **2017**, *29*, 1604431.
- [28] S. D. Stranks, G. E. Eperon, G. Grancini, C. Menelaou, M. J. P. Alcocer, T. Leijtens, L. M. Herz, A. Petrozza, H. J. Snaith, *Science* **2013**, *342*, 341.
- [29] D. Shi, V. Adinolfi, R. Comin, M. Yuan, E. Alarousu, A. Buin, Y. Chen, S. Hoogland, A. Rothenberger, K. Katsiev, Y. Losovyj, X. Zhang, P. A. Dowben, O. F. Mohammed, E. H. Sargent, O. M. Bakr, *Science* **2015**, *347*, 519.
- [30] Q. Dong, Y. Fang, Y. Shao, P. Mulligan, J. Qiu, L. Cao, J. Huang, *Science* **2015**, *347*, 967.
- [31] L. Shen, Y. Fang, D. Wang, Y. Bai, Y. Deng, M. Wang, Y. Lu, J. Huang, *Adv. Mater.* **2016**, *28*, 10794.
- [32] Y. Liu, Y. Zhang, Z. Yang, D. Yang, X. Ren, L. Pang, S. (F.) Liu, *Adv. Mater.* **2016**, *28*, 9204.
- [33] Y. Zhang, Y. Liu, Y. Li, Z. Yang, S. (F.) Liu, *J. Mater. Chem. C* **2016**, *4*, 9172.
- [34] M. I. Saidaminov, M. A. Haque, J. Almutlaq, S. Sarmah, X.-H. Miao, R. Begum, A. A. Zhumekenov, I. Dursun, N. Cho, B. Murali, O. F. Mohammed, T. Wu, O. M. Bakr, *Adv. Opt. Mater.* **2017**, *5*, 1600704.
- [35] H.-S. Rao, W.-G. Li, B.-X. Chen, D.-B. Kuang, C.-Y. Su, *Adv. Mater.* **2017**, *29*, 1602639.
- [36] Z. Chen, Q. Dong, Y. Liu, C. Bao, Q. Wang, X. Xiao, Y. Fang, Y. Bai, Y. Deng, J. Huang, unpublished.
- [37] Y. Fang, H. Wei, Q. Dong, J. Huang, *Nat. Commun.* **2017**, *8*, 14417.
- [38] Y. Shao, Z. Xiao, C. Bi, Y. Yuan, J. Huang, *Nat. Commun.* **2014**, *5*, 5784.
- [39] C. T. Lin, Y. K. Su, S. J. Chang, H. T. Huang, S. M. Chang, T. P. Sun, *IEEE Photonics Technol. Lett.* **1997**, *9*, 232.
- [40] J.-M. Liu, *Photonic Devices*, Cambridge University Press, Cambridge, UK **2005**.